TITLE: Predicting low frequencies in transition zone environments: state-of-the-art technologies and key limitations

Authors:

- *Jeremy Aznar, Julien Large, Philippe Herrmann, Thibaut Allemand et Baptiste Le Foulgoc, Sercel*
- *Shuki Ronen, Stanford / Sercel*
- *Stéphanie Chaillat, POEMS (CNRS-INRIA-ENSTA), Institut Polytechnique de Paris*
- *Luiz Maltez Faria, POEMS (CNRS-INRIA-ENSTA), Institut Polytechnique de Paris*
- *Eric Dunham, Stanford*

GEOPHYSICAL CONTEXT AND KEY CHALLENGES

The growing demand for marine seismic sources radiating down to about 1 Hz has renewed interest in source concepts capable of improving deep illumination and stabilizing broadband imaging and full-waveform inversion (FWI). The need is particularly acute in transition-zone and shallow-water environments, where the water column acts as a narrow, highly variable waveguide. In such settings, free-surface ghosts, bathymetry, and near-surface heterogeneity interact on time scales comparable to source emission, making low-frequency source characterization both critical and difficult. Low frequencies are essential for long-wavelength velocity updates and early-stage FWI, but they are also highly sensitive to source-wavelet uncertainty, attenuation, and coupling errors. As a result, inaccuracies in the 1–5 Hz band may be mapped into spurious updates in velocity, attenuation, coupling, or anisotropy. Accurate source characterization is therefore required not only for survey design and imaging quality, but also for amplitude-preserving processing and quantitative inversion. Combined with near-field measurements, source modeling also provides a practical means of monitoring source performance during acquisition. Among recent low-frequency source concepts, the Tuned Pulse Source (TPS) has emerged as a promising alternative. In contrast with Conventional Air Guns (CAG), which typically have chamber volumes of 45–520 cu in (0.7–8.5 L) and firing pressures of 2–3 kpsi (138–207 bar), this large-volume source operates with much larger volumes, on the order of 28 kcu in (459 L), and lower firing pressures (1000 psi (69 bar)), producing a bubble of about 5 m in diameter and a significantly longer release time. These dimensions place the source in a different physical regime from that of CAG. This study therefore asks whether conventional spherical lumped-parameter source models remain valid for such large-scale sources in shallow-water settings, and, if not, when higher-fidelity non-spherical modeling becomes necessary.

MARINE SOURCE SIGNATURES: PHYSICS, MODELING, AND PRACTICE

Air guns used for marine seismic surveys operate by rapidly releasing high-pressure air into the water, creating an oscillating bubble that radiates acoustic waves. The acoustic signature of the source is governed by thermodynamic bubble oscillation, which corresponds to the volumetric changes of the air bubble formed when the air gun discharges. The dominant bubble frequency is mainly controlled by chamber volume, firing pressure, and source depth, as described by Rayleigh–Willis type formulations. CAGs are generally deployed in arrays or clusters, and their collective wavefield is complex, involving source directivity as well as surface and seafloor reflections, as illustrated in Figure 1. For these reasons, marine source modeling has long been the subject of extensive investigation, from early simplified formulations (Herring, 1941; Cole, 1948; Gilmore, 1952; Ziolkowski, 1970; Vokurka, 1986; de Graaf et al., 2014; Watson et al., 2016) to increasingly sophisticated approaches now implemented in commercial software and calibrated using dedicated source-signature measurements. Even for conventional sources, the spherical bubble assumption is only approximate. As shown in Figure 2, during the early stage of bubble formation in a CAG, air is released through several discharge ports, generating an initially lobed, clover-shaped bubble rather than a perfectly spherical one. Although the bubble evolves toward a more rounded geometry at later times, its initial development is clearly non-spherical. In this work, a lumped-parameter bubble and air-gun model is first introduced and its applicability to large-scale source configurations is assessed. A Boundary Element Method (BEM) formulation is then presented, and the

conditions under which such an advanced approach becomes necessary to capture strongly non-spherical bubble dynamics and free-surface interaction are discussed.

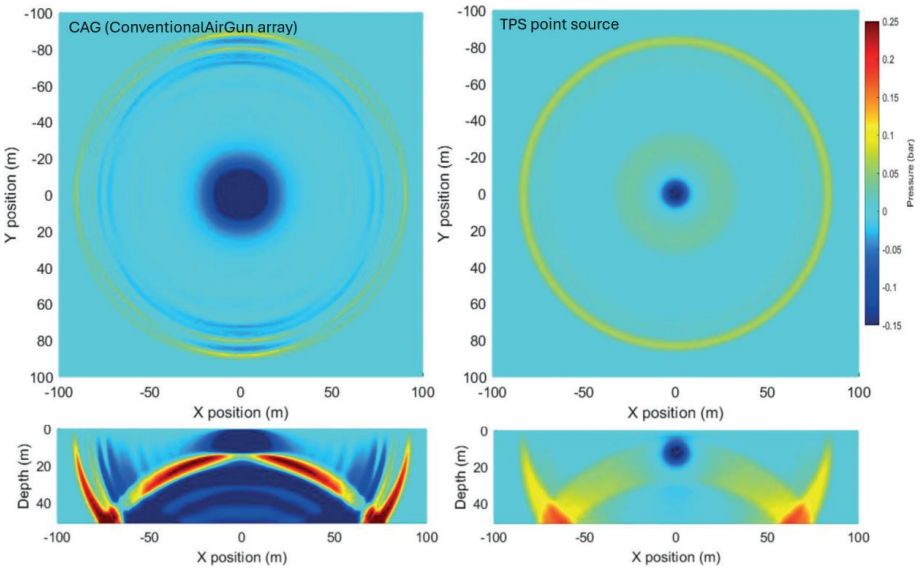


Figure 1. *Wave-propagation maps for a point source (right) and a CAG array (left), shown in top and side views. Interference from sea-surface ghosts and seafloor reflections is visible in both cases. This complexity is further increased for the array owing to source directivity.*

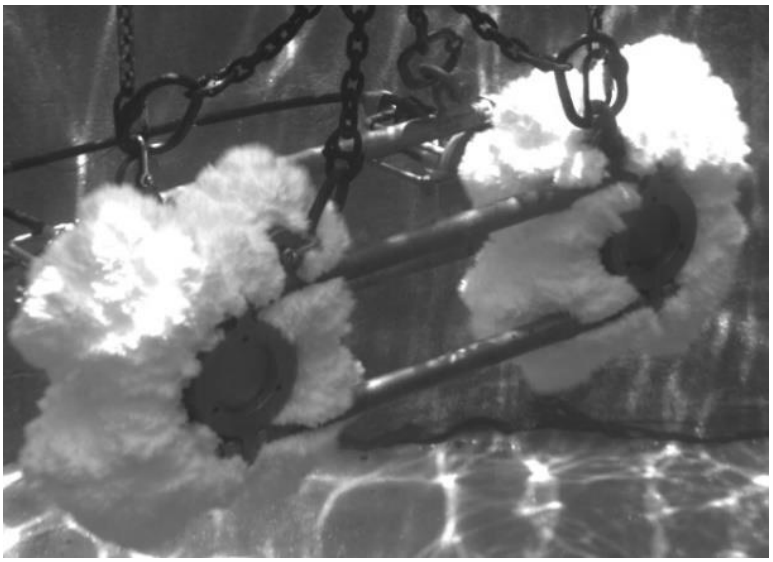


Figure 2. *Early-stage bubble formation for a CAG. Air is released through four discharge ports, generating an initially lobed, clover-shaped bubble rather than a perfectly spherical one. Although the bubble evolves toward a more rounded geometry at later times, its initial development is clearly non-spherical, showing that the spherical bubble assumption is already an approximation even for conventional sources.*

LUMPED PARAMETER BUBBLE AND AIR GUN MODEL

Overview of the model

This section describes the lumped-parameter model used to compute the acoustic pressure radiated by the oscillating bubble generated by an airgun discharge. The air gun and bubble are each represented by spatially uniform (but time-dependent) thermodynamic variables, and the surrounding water is modeled as a compressible liquid governed by the Tait equation of state. Provided the bubble is assumed spherical, the coupled airgun/bubble system can be written as a system of Ordinary Differential Equations (ODEs), which can be integrated efficiently in time and applied to both CAG sources and large-scale source configurations. For clarity, the source is represented by three coupled subsystems: firing chamber, port region, and bubble, as illustrated schematically in Figure 3. Detailed derivation is not the main focus here. Instead, the goal is to make explicit the physical assumptions of the model, especially those that may break down at large scale. This is why the full formulation used in the present work, including chamber depressurization, gas discharge through the port, bubble thermodynamics, and time integration, is given in Appendix A.

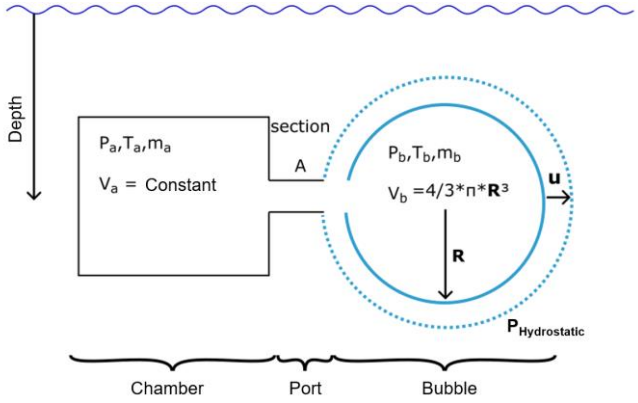


***Figure 3**. Schematic of the lumped-parameter air gun model. The source is represented by three coupled subsystems: the firing chamber, the port, and the oscillating bubble. Mass, pressure, and energy exchanges between these elements govern the emitted acoustic signal.*

Hydrostatic reference pressure and spherical-bubble assumption

In the spherical lumped-parameter model, a single ambient hydrostatic pressure is defined at the bubble-center depth,

$$P_{hydro} = P_{atm} + \rho_w g D, \qquad (1)$$

where D is the depth of the bubble center. This pressure serves as the reference far-field pressure for the surrounding liquid. The use of a single hydrostatic reference is a central simplification of the model, since it assumes that hydrostatic pressure variations across the vertical extent of the bubble remain small.

The surrounding water is described as a compressible liquid governed by the Tait equation of state,

$$\frac{P + B}{P_{hydro} + B} = \left(\frac{\rho}{\rho_\infty}\right)^n, \qquad (2)$$

where P and ρ are the local pressure and density in the liquid, ρ_∞ is the ambient density, and B and n are the Tait parameters. In this formulation, the liquid response is therefore referenced to a single ambient pressure evaluated at the bubble center.

The gas inside the bubble is described by the ideal-gas equation of state,

$$P_b = \frac{m_b R_{gas} T_b}{V_b}, \qquad (3)$$

where P_b, m_b, and T_b denote the bubble pressure, mass, and temperature, respectively. Under the spherical-bubble assumption, the bubble volume is

$$V_b = \frac{4}{3}\pi R^3, \qquad (4)$$

so that the entire bubble dynamics are reduced to the evolution of a single scalar radius $R(t)$. In practice, bubble thermodynamics are commonly closed using an effective polytropic law,

$$P_b V_b^{\gamma} = const. \qquad (5)$$

These relations highlight two key geometric simplifications. First, the bubble is represented by a single radius, which excludes shape deformation and assumes radially symmetric motion. Second, the surrounding liquid is referenced to a single hydrostatic pressure evaluated at the bubble center, which neglects vertical pressure differences across the bubble. Whether these assumptions remain acceptable on a large scale is the main question addressed below.

Compact system form and relevance to large-scale limitations

The detailed development of the lumped-parameter formulation is reported in Appendix A. In compact form, the coupled chamber-port-bubble dynamics are written as a system of ordinary differential equations for the state vector,

$$\frac{dY}{dt} = \{\dot{R}, \ddot{R}, \dot{P}_b, \dot{m}_b, \dot{T}_b, \dot{E}_b, \dot{P}_a, \dot{m}_a, \dot{T}_a, \dot{E}_a\}. \qquad (6)$$

This system is integrated in time using a classical explicit fourth-order Runge-Kutta scheme. The present reduced-order model provides a practical and computationally efficient description of conventional source behavior. At large scale, however, its limitations follow directly from the assumptions highlighted above: a single hydrostatic reference pressure, a spherical bubble geometry, and spatially uniform thermodynamic states. These assumptions are likely to become unreliable when the bubble diameter becomes comparable to the source depth, when buoyancy and hydrostatic gradients distort the bubble shape, and when strong free-surface interaction develops. The next section examines these effects from a scaling perspective.

A NEW SCALE OF SEISMIC SOURCES

Concept and motivation

We now turn to the TPS, a specially designed marine seismic source aimed at enhancing low-frequency signal while maintaining control over the emitted wavefield. It consists of a large volume source (28kcu in, 459 L) engineered to generate a signature with dominant energy at lower frequencies than CAG arrays. As shown in Figure 4, the first bubble harmonic is shifted to about 2.5–3 Hz for the large-volume source, compared with about 9–11 Hz for a conventional 150 cu in air gun, with significant signal content extending down to about 0.5 Hz. This shift is

directly related to the much larger oscillating air volume, which produces a primary bubble of 4 to 5 m in diameter. Because this low-frequency content is particularly valuable for waveform-based inversion and quantitative imaging, source characterization for such a large-scale source places stringent demands on source modeling. This single-point source is omnidirectional in the far field and thus allows a better and more robust wavelet definition for postprocessing and inversion. These large-scale, low-frequency bubbles raise questions about the validity of the spherical, lumped-parameter model described in Section 2, particularly at shallow towing depths.

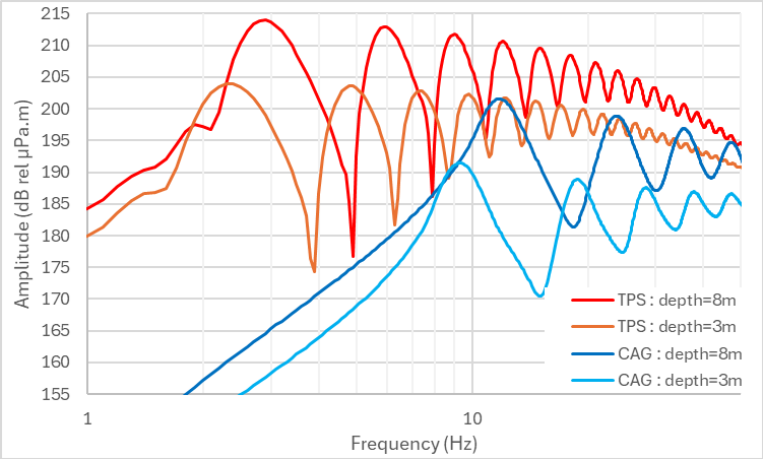


Figure 4 *Frequency-domain acoustic signatures of a CAG and of the large-volume source. The first bubble harmonic is observed around 2.5–3 Hz for the large-volume source, compared with about 9–11 Hz for a 150 cu in CAG, highlighting the enhanced low-frequency content of the large-scale source.*

Change of scale relative to CAG

This change of scale in bubble size for the large-volume source is expected to have a significant effect on the bubble shape and thus on the validity of the spherical bubble assumption. The larger vertical extent of the bubble enhances hydrostatic pressure gradients, making the pressure at the bottom of the bubble noticeably higher than at the top. As a consequence, the difference in hydrostatic pressure between the top and bottom of the bubble is at least twice as large for the large-volume source as for a CAG bubble. This increased pressure contrast promotes shape distortions and asymmetries that are not well captured by simple spherical models. Because buoyancy scales with bubble volume, and thus with the cube of the bubble radius, the Archimedean force acting on a large-scale source bubble is expected to be about 10–20 times greater than for a CAG bubble. By contrast, the rise velocity shows a much weaker dependence on size. Experimental observations indicate an increase of only about 1.5–2 for the large-volume source, consistent with simple drag-based scaling. These figures should be viewed as order-of-magnitude estimates, as the actual bubble dynamics are also influenced by deformation, oscillation, added mass, and free-surface interaction. The main scaling differences between CAG and the large-scale source studied here are summarized in Table 1.

	TPS	CAG
Single unit volume (cuin)	28 000	45-520
First harmonic (Hz)	2.5-2.9	7-12
Bubble radius (m)	2-2.5	0.5-1
Towing depth (m)	3-8	3-8
Hydrostatic pressure difference (bar)	0.4-0.5	0.05-0.1
Towing depth / Bubble radius	1.2-4	3-16
Pulse width (ms)	50-60	10-20
Ghost delay (ms)	4-11	4-11
Buoyancy force (kN)	330-640	5-40

Table 1. *Comparison of characteristic parameters for large-volume source and CAG. This table highlights the main scale differences between the two source types, including source volume, bubble radius, first harmonic, hydrostatic pressure gradient across the bubble, towing-depth-to-bubble-radius ratio, pulse width, ghost delay, and Archimedean buoyancy force.*

Shallow towing depth and free-surface interaction

For the large-volume source, the ratio between bubble diameter and towing depth is much larger than for CAG, placing the source close to the regime where near-surface effects and free-surface interactions become important. The resulting proximity of the large bubble to the water–air interface strengthens the impact of hydrostatic pressure gradients and surface-reflected waves, making the assumption of an isolated spherical bubble increasingly questionable. In this context, the experiments of Wehner et al. (2019) provide key constraints on model validity at shallow depths. They show that spherical bubble models start to fail when the source depth is less than about 1.5 times the bubble radius, with marked discrepancies in the low-frequency part of the signature due to strong free-surface interaction. Because the large-scale source operates with a much larger bubble radius at similar towing depths, it naturally approaches or enters this critical regime. Although the experiments by Wehner et al. were conducted on relatively small sources very close to the surface, the difference in scale for the large-volume source does not invalidate their conclusions. On the contrary, their findings strongly suggest that free-surface interaction may become a dominant limitation for such large-scale bubbles as well, particularly for predicting the low-frequency response. In addition, when the bubble reaches the free surface, the oscillations are effectively quenched, which abruptly terminates the bubble pulse. This termination mechanism is not accounted for in standard spherical bubble models, and it becomes increasingly important for such large-scale sources because of their long oscillation period, large bubble size, and rapid vertical rise. This scale effect is quantified in Figure 5, which compares the time evolution of bubble radius (Figure 5a) and emitted acoustic pressure (Figure 5b) for a 150 cu in CAG and a 28 kcuin large-volume source at depths of 3 m and 8 m. A direct consequence is the stronger coupling between the source pulse and the free-surface ghost, as illustrated in Figure 6. For a CAG, the surface-reflected wave arrives after the main bubble pressure has already decayed, so its effect is largely confined to the later, lower-amplitude part of the signature. For the large-volume source, in contrast, the ghost arrives while the bubble pressure remains near its maximum, so that free-surface reflection interacts with the source during the energetically dominant part of the emission. In shallow-water large-scale source configurations, source dynamics and ghost

effects can therefore no longer be treated as weakly coupled, which strongly limits the validity of standard spherical models.

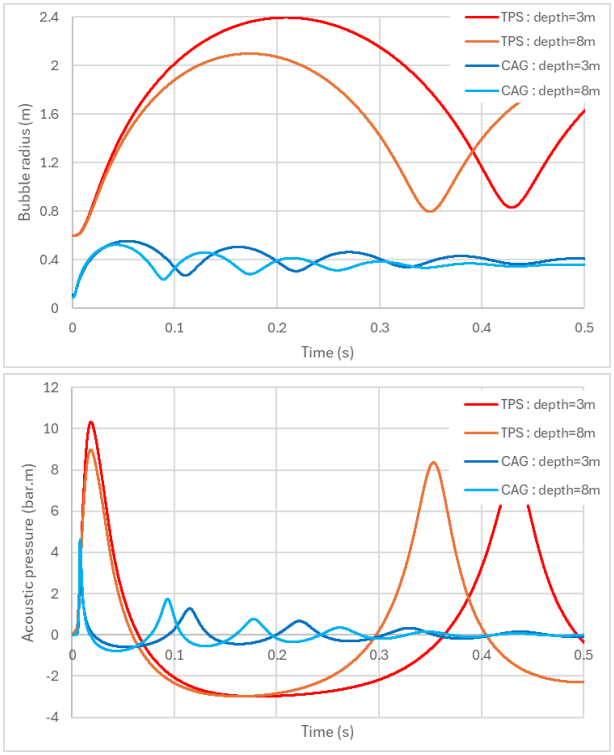


***Figure 5**. Bubble radius (a) and emitted acoustic pressure (b) versus time for a 150 cu in CAG and the large-volume source at source depths of 3 m and 8 m. The large-volume source exhibits much larger bubble excursions and a longer oscillation period, highlighting the change in physical scale relative to conventional sources.*

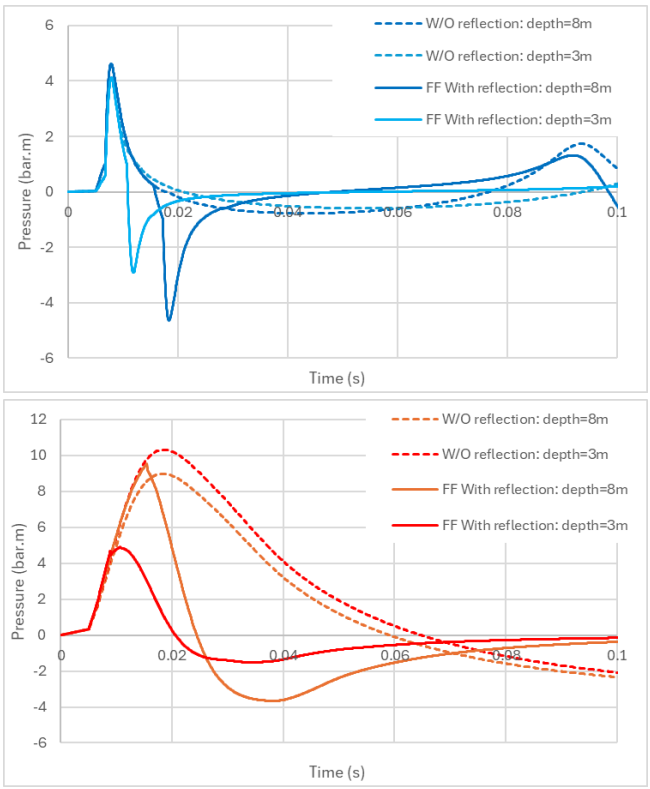


Figure 6. *Notional (without ghost) and far-field (with ghost) acoustic pressure for the CAG (a) and the large-volume source (b). For the CAG, the ghost arrives after the main bubble pressure has decayed, whereas for the large-volume source it overlaps with the pressure maximum, producing much stronger source–ghost interaction.*

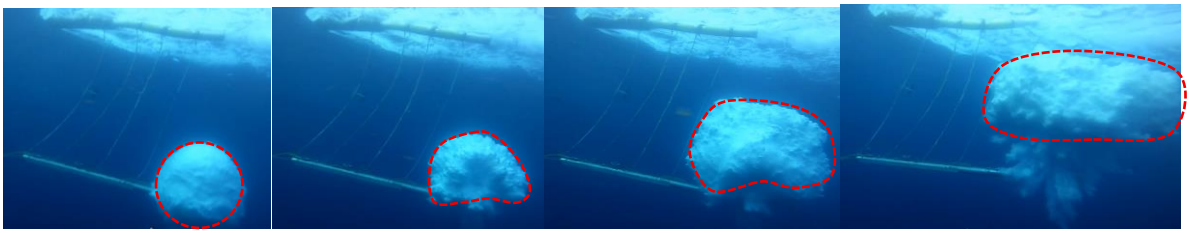


Figure 7. *Evolution of the large-volume source bubble over time. The bubble shape evolves from nearly spherical at early times to increasingly flattened at later times. This deformation is attributed to scale-related effects discussed in this section, notably hydrostatic pressure gradients, buoyancy, and free-surface interaction.*

TOWARD NONSPHERICAL BUBBLE SIMULATIONS: MATHEMATICAL MODELING WITH BOUNDARY INTEGRAL EQUATIONS

When the bubble is assumed to be spherical, the problem can be described using a relatively simple system of ODEs, which makes it possible to obtain accurate and stable solutions without major difficulty. By contrast, three-dimensional non-spherical bubbles involve much more complex challenges, which we investigate here. Since our goal is to explore three-dimensional effects on the bubble dynamics and its impact on the acoustic signature, we simplify some of the physical assumptions and ignore both viscous and surface tension effects in the discussion that follows. Before presenting the numerical method to simulate these complex bubbles, let us recall the governing equations to fix the assumptions and notations. We consider a gas bubble $\Omega_b(t) \subset \mathbb{R}^3$immersed in a liquid occupying $\Omega_f(t) = \mathbb{R}^3 \setminus \overline{\Omega_b(t)}$. The bubble boundary $\Gamma(t) = \partial\Omega_b(t)$ is a closed smooth surface with outward unit normal pointing into the liquid and $V_b(t)$ denotes the bubble volume. We take z to be the upward vertical coordinate and e_z the corresponding unit vector.

The liquid is modeled as incompressible and inviscid, with constant density ρ. Its velocity field u satisfies Euler's equations,

$$\rho\left(\frac{\partial u}{\partial t} + (u \cdot \nabla)u\right) = -\nabla p - \rho g e_z \quad \text{in } \Omega_f(t)$$
$$\nabla \cdot u = 0 \quad \text{in } \Omega_f(t)$$

complemented by the requirement that the velocity tends to zero at infinity.

We further assume the flow to be irrotational. Under this assumption the velocity derives from a scalar potential ϕ, such that $u = \nabla\phi$, and the incompressibility constraint reduces to

$$\Delta\phi = 0 \quad \text{in } \Omega_f(t)$$

complemented by the requirement that the potential gradient tends to zero at infinity.

For irrotational flow, the convective term simplifies, which allows the momentum equation to be written in a conservative form. Using far-field conditions, this leads to the unsteady Bernoulli equation where the sum of kinetic, pressure, and gravitational potential terms is spatially uniform

$$\frac{\partial \phi}{\partial t} + \frac{1}{2}|\nabla \phi|^2 + \frac{p - p_{\text{ref}}}{\rho} + gz = 0$$

We can now derive the boundary conditions on the bubble surface. The **kinematic condition** follows from the fact that the bubble interface is a material surface: every point moves with the local fluid velocity

$$\frac{Dx}{Dt} = \nabla \phi(x, t), \qquad x \in \Gamma(t)$$

Evaluating Bernoulli's equation on the bubble boundary and introducing the pressure jump condition gives the **dynamic boundary condition**

$$\frac{D\phi}{Dt} = \frac{1}{2}|\nabla \phi|^2 + B(p_b, x), \qquad x \in \Gamma(t)$$

where

$$B(p_b, x) \coloneqq \frac{p_{\text{ref}} - p_b}{\rho} - gz - \frac{[p]}{\rho}$$

The bubble pressure is related to its volume through an equation of state, written in abstract form as $F(V_b, p_b) = 0$

Given the initial data, the complete evolution problem consists in finding the potential, the bubble pressure, and the surface such that:

$$\Delta \phi = 0 \quad \text{in } \Omega_f(t)$$

$$\frac{D\phi}{Dt} = \frac{1}{2}|\nabla \phi|^2 + B(p_b, x) \quad \text{on } \Gamma(t)$$

$$\frac{Dx}{Dt} = \nabla \phi \quad \text{on } \Gamma(t)$$

$$F(V_b, p_b) = 0$$

At each time step the kinetic and dynamic boundary conditions in the previous system require the gradient of ϕ and the Dirichlet data φ on the current bubble surface. We compute this via a boundary integral equation on Γ. For a fixed time t, we seek ϕ satisfying the exterior Dirichlet problem

$$\Delta \phi = 0 \quad \text{in } \Omega_f$$

$$\phi = \varphi \quad \text{on } \Gamma$$

Boundary integral methods provide a natural and efficient framework for solving exterior problems, as they reduce the formulation to the boundary. Accordingly, the system can be

reformulated as a boundary integral equation defined solely on the bubble surface, using the three-dimensional Laplace Green's function.

$$G(x,y) = \frac{1}{4\pi|x-y|}$$

Green's functions allow for several equivalent boundary integral formulations. Here, we adopt the simplest one, based on the single-layer potential, which reads:

$$\varphi(x) = \int_{\Gamma} G(x,y)\phi(y)dS(y)$$

To reduce computational costs, axisymmetric three-dimensional formulations have been successfully employed to simulate gas bubbles (add reference), while fully non-axisymmetric simulations have also been proposed (Li, 2020; Bui, 2006). While BEM are highly efficient for exterior problems, most existing work has focused on fixed geometries. In bubble dynamics, however, geometry evolves in time, requiring solvers that can efficiently adapt to these changes. Fast BEM methods developed for large-scale problems are generally not designed to handle such evolving geometries.

A key challenge is thus maintaining stability over time. The coupling between the evolving geometry and the accuracy of the BEM solution leads to error accumulation. Several stabilization strategies have been proposed to address these issues (Bui, 2006; Li, 2020). However, such approaches often introduce a smoothing effect, raising the question of whether the computed solution corresponds to the original problem or to an effectively regularized (smoothed) one. From a mathematical standpoint, a natural question is whether the observed stability issues are intrinsic to spherical solutions being linearly unstable for in the parameter regime considered (Plesset, 1954), in which case the deviations from a spherical geometry in multidimensional simulations is a feature of the mathematical model, and not necessarily a sign of numerical (and unphysical) instabilities. An important challenge is also the development of numerical methods that avoid any ad hoc parameter tuning.

Another important research direction concerns the behavior of gas bubbles in shallow water environments. The main additional difficulty for BEMs lies in the simultaneous incorporation of two boundary conditions. While free-surface or seabed effects can often be incorporated in a relatively straightforward way through appropriate Green's functions, the situation is much less clear in the presence of waveguide-type boundary conditions. Addressing this problem could significantly impact the modeling of gas bubbles and potentially open new directions for research within the BEM community.

CONCLUSION

TPS source modeling brings marine seismics into a regime where the assumptions underlying conventional spherical lumped-parameter models become increasingly fragile. At the large bubble scales targeted for ultra-low-frequency emission, and even more so at the very shallow towing depths required in transition-zone settings, buoyancy, hydrostatic pressure gradients, and free-surface interaction are expected to play a first-order role. These effects may modify the emitted signature and limit the validity of standard spherical formulations. This is precisely the regime in which low-frequency signature fidelity is most critical for quantitative imaging and

waveform-based inversion. To date, large-volume sources have not yet been deployed in transition-zone environments. The present work therefore provides a priori physics-based assessment of the physical and mathematical limitations of standard modeling approaches in the configurations where a large-volume source is expected to be most challenging and most valuable. It also motivates the use of higher-fidelity approaches, such as Boundary Element Methods, to capture non-spherical bubble dynamics and strong boundary coupling. Experimental deployments planned in such environments before the end of the year should provide the first data specifically suited to test these hypotheses and to validate the corresponding models. This upcoming confrontation between modeling and field observations will be essential to establish a predictive framework for large-volume source characterization in shallow-water and transition-zone applications.

APPENDIX

Air-gun chamber

As described by Leighton et al. (2019), in the lumped-parameter air-gun model, we track the pressure P_a, mass m_a, temperature T_a, and internal energy $E_a$of the gas in the firing chamber. The gun volume is denoted by V_a. The gas is assumed to obey the ideal-gas equation of state,

$$P_a = \frac{m_a R_{\text{gas}} T_a}{V_a}, \qquad \text{(A1)}$$

where $R_{\text{gas}}$is the specific gas constant, and the internal energy is

$$E_a = c_v m_a T_a, \qquad \text{(A2)}$$

with $c_v$the specific heat at constant volume. The heat capacity at constant pressure is $c_p = \gamma c_v$, where γ is the ratio of specific heats.

When the port is open, mass flows from the air-gun chamber into the bubble through an orifice of area A. The mass flow rate is described by a classical compressible-flow formulation (Barré-de Saint-Venant type), distinguishing between subsonic (unchoked) and choked flow. We denote the upstream reservoir by the air gun $(P_a, T_a, m_a)$and the downstream reservoir by the bubble (P_b, T_b, m_b).

For subsonic flow, when

$$\frac{P_b}{P_a} \geq \left(\frac{2}{\gamma+1}\right)^{\gamma/(\gamma-1)}, \qquad \text{(A3)}$$

the mass flow rate into the bubble is

$$\frac{dm_b}{dt} = P_a A \left(\frac{1}{R_{\text{gas}} T_a}\right)^{1/2} \left(\frac{2\gamma}{\gamma-1}\right)^{1/2} \sqrt{\left(\frac{P_b}{P_a}\right)^{2/\gamma} - \left(\frac{P_b}{P_a}\right)^{(\gamma+1)/\gamma}}, \qquad \text{(A4)}$$

For choked (sonic) flow, when

$$\frac{P_b}{P_a} < \left(\frac{2}{\gamma+1}\right)^{\gamma/(\gamma-1)}, \qquad \text{(A5)}$$

the mass flow rate is

$$\frac{dm_b}{dt} = P_a A \left(\frac{1}{R_{\text{gas}} T_a}\right)^{1/2} \left(\frac{2\gamma}{\gamma+1}\right)^{1/2} \left(\frac{2}{\gamma+1}\right)^{1/(\gamma-1)}. \qquad \text{(A6)}$$

Mass conservation across the port implies $\dot{m}_a = -\dot{m}_b$, while the chamber internal energy is updated from the enthalpy flux associated with gas discharge:

$$\frac{dE_a}{dt} = c_p T_a \frac{dm_a}{dt}, \qquad \text{(A7)}$$

and the temperature and pressure are updated consistently with equations (A1)-(A2). For later use, the pressure rate can be written in compact form as

$$\frac{dP_a}{dt} = \frac{R_{\text{gas}}}{V_a}\left(T_a \frac{dm_a}{dt} + m_a \frac{dT_a}{dt}\right). \qquad \text{(A8)}$$

The local speed of sound in the gas is given by the ideal-gas relation

$$c_g = \sqrt{\gamma P/\rho} = \sqrt{\gamma R_{\text{gas}} T}, \qquad \text{(A9)}$$

which is consistent with the compressible-flow relations used above (e.g., Chapman, 2000; Babu, 2014).

Bubble dynamics and thermodynamics

The bubble is idealized as spherically symmetric, with spatially uniform internal properties. Its radius and wall velocity are denoted by $R(t)$ and $\dot{R}(t)$. In the spherical lumped-parameter model, we define a single ambient hydrostatic pressure at the bubble center,

$$P_{\text{hydro}} = P_{\text{atm}} + \rho_w g D, \qquad \text{(A10)}$$

where D is the bubble-center depth and ρ_w is the water density. This pressure plays the role of the reference far-field pressure in the Tait equation and enthalpy definition. This approximation is one of the key assumptions whose validity is reassessed later for large-scale bubbles, whose vertical extent may become comparable to the source depth.

The surrounding water is modeled as a compressible liquid governed by the Tait equation of state:

$$\frac{P + B}{P_{\text{hydro}} + B} = \left(\frac{\rho}{\rho_\infty}\right)^n, \qquad \text{(A11)}$$

where P and ρ are the local pressure and density, ρ_∞ is the ambient density, B is the Tait constant, and n is the Tait exponent. From equation (A11), the local sound speed in the liquid is

$$c_l = c_\infty \left(\frac{P_b + B}{P_{\text{hydro}} + B}\right)^{(n-1)/2n}, \qquad \text{(A12)}$$

where P_b is the gas pressure inside the bubble and c_∞ is the sound speed at ambient conditions. The bubble-wall dynamics are governed by the Gilmore equation with empirical damping terms:

$$\ddot{R} = \frac{H(1+\dot{R}/c_l) + R\dot{H}(1-\dot{R}/c_l)/c_\infty - \frac{3}{2}\dot{R}^2(1-\dot{R}/3c_l) - \alpha\dot{R} + \beta\dot{R}^2}{R(1-\dot{R}/c_l)}, \qquad \text{(A13)}$$

where H is the enthalpy difference in the liquid, and α and β are empirically determined damping coefficients introduced to account for unmodeled dissipation mechanisms (e.g., turbulence, phase change). In practice, these coefficients are treated as effective calibration parameters. The enthalpy difference between the bubble-wall pressure P_b and the reference ambient pressure is

$$H = \int_{P_{\mathrm{hydro}}}^{P} \frac{dp}{\rho} = \frac{n(P_{\mathrm{hydro}}+B)}{(n-1)\rho_\infty}\left[\left(\frac{P_b+B}{P_{\mathrm{hydro}}+B}\right)^{(n-1)/n} - 1\right], \qquad \text{(A14)}$$

and its time derivative, entering equation (A13), is written as

$$\dot{H} = \frac{\dot{P}_b}{\rho_\infty}\left(\frac{P_b+B}{P_{\mathrm{hydro}}+B}\right)^{-1/n}. \qquad \text{(A15)}$$

The gas in the bubble is described as an ideal gas with internal energy E_b, mass m_b, temperature T_b, and volume $V_b = 4\pi R^3/3$. The equation of state is

$$P_b = \frac{m_b R_{\mathrm{gas}} T_b}{V_b}, \qquad \text{(A16)}$$

and the internal energy is

$$E_b = c_v m_b T_b. \qquad \text{(A17)}$$

In practice, the thermodynamic evolution of the bubble can be expressed either via a polytropic law of the form

$$P_b V_b^\gamma = \text{const.}, \qquad \text{(A18)}$$

or via a full energy balance analogous to that used for the air gun, possibly including heat transfer to the surrounding water. In the present implementation, we use an effective polytropic behavior (equation A18), with γ chosen to account for non-adiabatic effects in an average sense.

Acoustic radiation

The oscillatory expansion and contraction of the bubble drive acoustic waves in the water. We describe the bubble as a monopole source and use a Landrø-type expression for the radiated pressure at an observation distance r_{obs} in the far field,

$$p(r_{\mathrm{obs}}, t) - P_{\mathrm{hydro}} = \rho_\infty \frac{R(t)}{r_{\mathrm{obs}}}\left(H(t) + \frac{\dot{R}(t)^2}{2}\right), \qquad \text{(A19)}$$

with $H(t)$ given by equation (A14). This formulation provides a direct link between the bubble dynamics computed from equation (A13) and the acoustic pressure recorded at a receiver.

State vector and time integration

For convenience, the ten state variables are gathered in a vector and the corresponding time derivatives dY/dt are

$$\frac{dY}{dt} = \{\dot{R}, \ddot{R}, \dot{P}_b, \dot{m}_b, \dot{T}_b, \dot{E}_b, \dot{P}_a, \dot{m}_a, \dot{T}_a, \dot{E}_a\}, \qquad \text{(A20)}$$

where:

- $\dot{R}$ is the bubble-wall velocity,
- $\ddot{R}$ is given by the Gilmore equation (equation A13),
- $\dot{m}_b$ is given by equations (A4) or (A6), depending on the flow regime (subsonic or choked),
- $\dot{m}_a = -\dot{m}_b$ by mass conservation across the port,
- $\dot{E}_a = c_p T_a \dot{m}_a$ from equation (A7),
- $\dot{E}_b$ and $\dot{T}_b$ follow from $E_b = c_v m_b T_b$ (equation A17) and $\dot{m}_b$; in the effective polytropic case, $\dot{T}_b$ is obtained by differentiating equation (A18),
- $\dot{P}_a$ is given by equation (A8),
- $\dot{P}_b$ is related to $\dot{m}_b$ and $\dot{T}_b$ via equation (A16),
- $\dot{H}$ is then computed from $\dot{P}_b$ using equation (A15).

The resulting system of ODEs is integrated in time using a classical explicit fourth-order Runge-Kutta scheme, with appropriate initial conditions for the air-gun and bubble variables. Source-specific parameters, including initial chamber pressure and temperature, initial bubble volume and pressure, gun depth, chamber volume, firing pressure, orifice-area history $A(t)$, and effective thermodynamic coefficients α, β, and γ, are based on measurements or calibration data.

REFERENCES

Leighton, M. Watson, Werpers, J., & Dunham, E. M., 2019, What controls the initial peak of an air-gun source signature?

Watson, L. M., Werpers, J., and Dunham, E. M., 2016, Towards a physics-based model of airgun arrays for seismic exploration: *Geophysics*

Wehner, D., Landrø, M., & Amundsen, L., 2019, On low frequencies emitted by air guns at very shallow depths — An experimental study.

Bui, T. T., Ong, E. T., Khoo, B. C., Klaseboer, E., & Hung, K. C., 2006, A fast algorithm for modeling multiple bubbles dynamics: *Journal of Computational Physics*, 216, 430–453, http://doi.org/10.1016/j.jcp.2005.12.009.

Cole, R. H., 1948, *Underwater explosions*: Princeton University Press, http://dx.doi.org/10.5962/bhl.title.48411.

de Graaf, K. L., Penesis, I., & Brandner, P. A., 2014, Modelling of seismic airgun bubble dynamics and pressure field using the Gilmore equation with additional damping factors: *Ocean Engineering*, 76, 32–39, http://dx.doi.org/10.1016/j.oceaneng.2013.12.001.

Gilmore, F. R., 1952, *The growth or collapse of a spherical bubble in a viscous compressible liquid*: Hydrodynamics Laboratory, California Institute of Technology, Technical Report.

Herring, C., 1941, *Theory of the pulsations of the gas bubble produced by an underwater explosion*: OSRD Report 236.

Li, S., van der Meer, D., Zhang, A.-M., et al., 2020, Modelling large scale airgun-bubble dynamics with highly non-spherical features: *International Journal of Multiphase Flow*, 122, 103143, **https://doi.org/10.1016/j.ijmultiphaseflow.2019.103143**.

Plesset, M.S., 1954. On the stability of fluid flows with spherical symmetry. *Journal of Applied Physics, 25(1),* pp. 96-98.

Vokurka, K., 1986, Comparison of Rayleigh's, Herring's, and Gilmore's models of gas bubbles: *Acta Acustica United with Acustica*, 59, 214–219.

Ziolkowski, A., 1970, A method for calculating the output pressure waveform from an air gun: *Geophysical Journal of the Royal Astronomical Society*, 21, 137–161, **http://dx.doi.org/10.1111/j.1365-246X.1970.tb01773.x**.

Babu, M. V., 2014, *Fundamentals of Gas Dynamics*: New Age International Publishers.